Scripta Materialia 250 (2024) 116184

Contents lists available at ScienceDirect

Scripta Materialia

journal homepage: www.journals.elsevier.com/scripta-materialia

Metastable phases in sputtered stoichiometric Co_3Al

Ke Xu [a], Zhongxia Shang [a], Xuanyu Sheng [a], Nicholas Richter [a], Anyu Shang [a], Chao Shen [a], Bo Yang [a], Yifan Zhang [a], Tongjun Niu [a], Haiyan Wang [a,b], Xinghang Zhang [a,*]

[a] School of Materials Engineering, Purdue University, West Lafayette, IN 47907, USA
[b] School of Electrical and Computer Engineering, Purdue University, West Lafayette, IN 47907, USA

ARTICLE INFO

Keywords:
Stoichiometric Co_3Al
Metastable phases
Lattice parameters
Stacking faults
Transmission electron microscopy

ABSTRACT

Co-Al based superalloys have been considered as the promising alternatives to Ni-Al based superalloys. Appropriate alloy design can stabilize a dual phase structure of face-centered cubic (FCC) Co matrix and $L1_2$ $Co_3(Al, X)$ intermetallics and avoid precipitation of B2 CoAl intermetallics for Co-Al based superalloys. It has been shown that stable Co_3Al single phase compound does not exist. Instead, at such a chemistry, Co-Al binary phase diagram predicts the coexistence of hexagonal close-packed (HCP) Co and B2 CoAl at room temperature. Here we report the synthesis of stoichiometric Co_3Al via magnetron sputtering. Transmission electron microscopy investigations identified metastable phases of Co_3Al, dominated by HCP supersaturation with minor $L1_2$ intermetallics. Furthermore, the phase transformation from HCP-to-FCC Co_3Al induced by stacking faults in Co/Co_3Al multilayers is also discussed. This investigation provides new insights on the crystal structures of stoichiometric Co_3Al and the design of novel Co-Al based alloy systems.

Co-Al based superalloys have been considered as one of the promising alternatives to Ni-Al based superalloys because of higher melting point, better high temperature durability and better welding performance [1]. However, unlike the strengthening precipitate phase in Ni-Al based superalloys, $L1_2$ Ni_3Al intermetallic, the single-phase Co_3Al compound does not exist as predicted by the Co-Al phase diagram. The phase equilibria for Co-25 at.% Al consist of either dual phases of B2 CoAl and hexagonal close-packed (HCP) Co below 298 °C or dual phases of B2 CoAl and face-centered cubic (FCC) Co above 298 °C, as shown in Fig. S1. There are extensive trial and error designs or density functional theory (DFT) calculations revealing the desirable $L1_2$ $Co_3(Al, X)$ intermetallics can be stabilized in certain Co-Al-X ternary systems, where X can be elements from transition groups such as W, Ta, Ti, V, Nb and Mo [2–8]. Nevertheless, few studies focused on the stabilization of binary stoichiometric Co_3Al compound itself, which is critical to the fundamental understanding of phase constituents and mechanical behaviors of Co-Al based alloys.

The phase stability of $L1_2$ $Co_3(Al, X)$ intermetallics has been extensively investigated experimentally and computationally [1,9]. The long-lasting thermal stability of $L1_2$ $Co_3(Al, X)$ is nonexistent. Upon long time aging at elevated temperatures, the dual phase microstructure of FCC Co matrix and $L1_2$ ordered intermetallics decomposed to the equilibrium phases consisting of FCC Co, B2 CoAl and $D0_{19}$ ordered Co_3X [1,5,10,11], even in multicomponent systems with addition of elements which have been considered to stabilize $L1_2$ Co_3Al intermetallics [2–8]. DFT calculations confirmed that $D0_{19}$ Co_3X phases are thermodynamically more stable under elevated temperatures compared to $L1_2$ $Co_3(Al, X)$ counterparts [12]. Recent studies also indicated that $L1_2$ $Co_3(Al, X)$ phases show continuous order-to-disorder transition accompanied with atomic site configuration change over a broad temperature range [13]. These prior studies imply the structural instability nature of $L1_2$ $Co_3(Al, X)$ intermetallics even in multicomponent systems. Therefore, fundamental investigations regarding the metastable crystal structures of stoichiometric Co_3Al are urgently needed to reveal the crystallographic nature of Co_3Al and improve the stability of $L1_2$ $Co_3(Al, X)$ intermetallics.

It is known that magnetron sputtering enabled the stabilization of supersaturated single phase, supersaturated solid solution with precipitates or metastable phases due to the extremely high quenching rates during sputtering process [14–23]. Textured or epitaxial nanoscale metallic multilayers can also be obtained via appropriately controlling substrates, seed layers and deposition conditions [24–25]. When the thickness of periodical multilayers reduces to several nanometers, metastable phases can be stabilized [26–30], as one of the layer constituents acts as template for the pseudomorphic stabilization of nonequilibrium phases in the adjacent layers [31]. Below the critical

* Corresponding author.
E-mail address: xzhang98@purdue.edu (X. Zhang).

https://doi.org/10.1016/j.scriptamat.2024.116184
Received 10 January 2024; Received in revised form 20 April 2024; Accepted 16 May 2024
Available online 30 May 2024

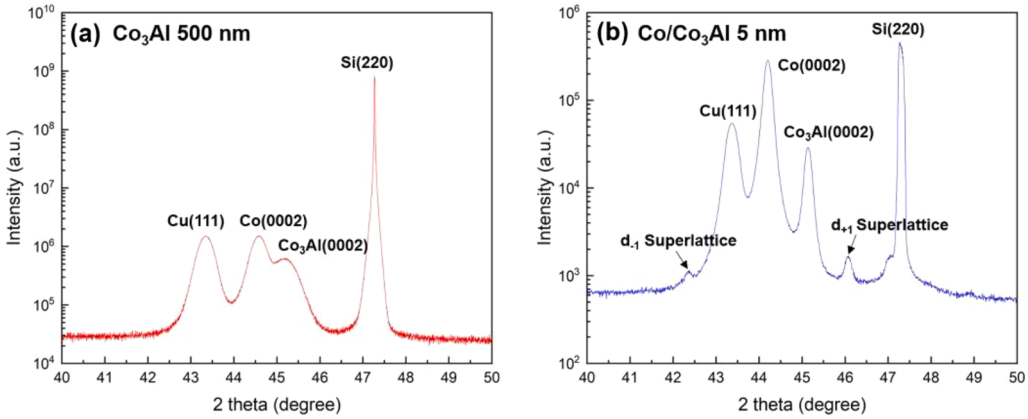

Fig. 1. (a) XRD pattern of as-deposited Co_3Al 500 nm/Co 50 nm/Cu 50 nm stacking on Si (110) substrate. (b) XRD pattern of as-deposited Co/Co_3Al 5 nm multilayers on Cu 50 nm seed layer on Si (110) substrate. The first order superlattices between Co_3Al (0002) and Co (0002) are labeled.

layer thickness, the interfacial energy or surface energy will be dominated over bulk free energy and strain energy, therefore encouraging the formation of metastable phase with low interfacial energy [32], as evidenced in metastable cubic AlN in AlN/TiN multilayers [33], metastable BCC Cu in Cu/Nb multilayers [34] and metastable body-centered cubic (BCC) Mg in Mg/Nb multilayers [31].

In this work, we report several metastable crystal structures in the sputtered stoichiometric Co_3Al. Transmission electron microscopy (TEM) studies reveal that $L1_2$ intermetallics are embedded in HCP supersaturated matrix in the as-deposited Co_3Al single layer films. The formation of FCC Co_3Al induced by stacking faults (SFs) was also captured in the as-deposited Co 5 nm/Co_3Al 5 nm multilayers. Our studies shed light on the metastable phases of Co_3Al and provide new possibilities for the design of novel Co-Al based alloys.

500 nm thick Co-25 at.% Al (referred to as Co_3Al hereafter) films were co-sputtered at room temperature using Co (99.95%) and Al (99.999%) targets on Co 50 nm/Cu 50 nm double seed layers onto HF etched Si (110) substrates in an AJA ATC-2200-UHV magnetron sputtering system. Prior to deposition, the sputter chamber's base pressure was 8×10^{-8} torr. Ar pressure was kept as 3.5 mtorr during deposition. Meanwhile Co 5 nm/Co_3Al 5 nm multilayers (referred to as Co/Co_3Al 5 nm multilayers hereafter) with a total film thickness of 150 nm were deposited on 50 nm Cu seed layer onto HF etched Si (110) substrates. The deposition conditions are the same as single layer Co_3Al films. X-ray diffraction (XRD) investigation was performed on Panalytical Empyrean X'pert PRO MRD diffractometer operated at 40 kV using Cu $K\alpha_1$

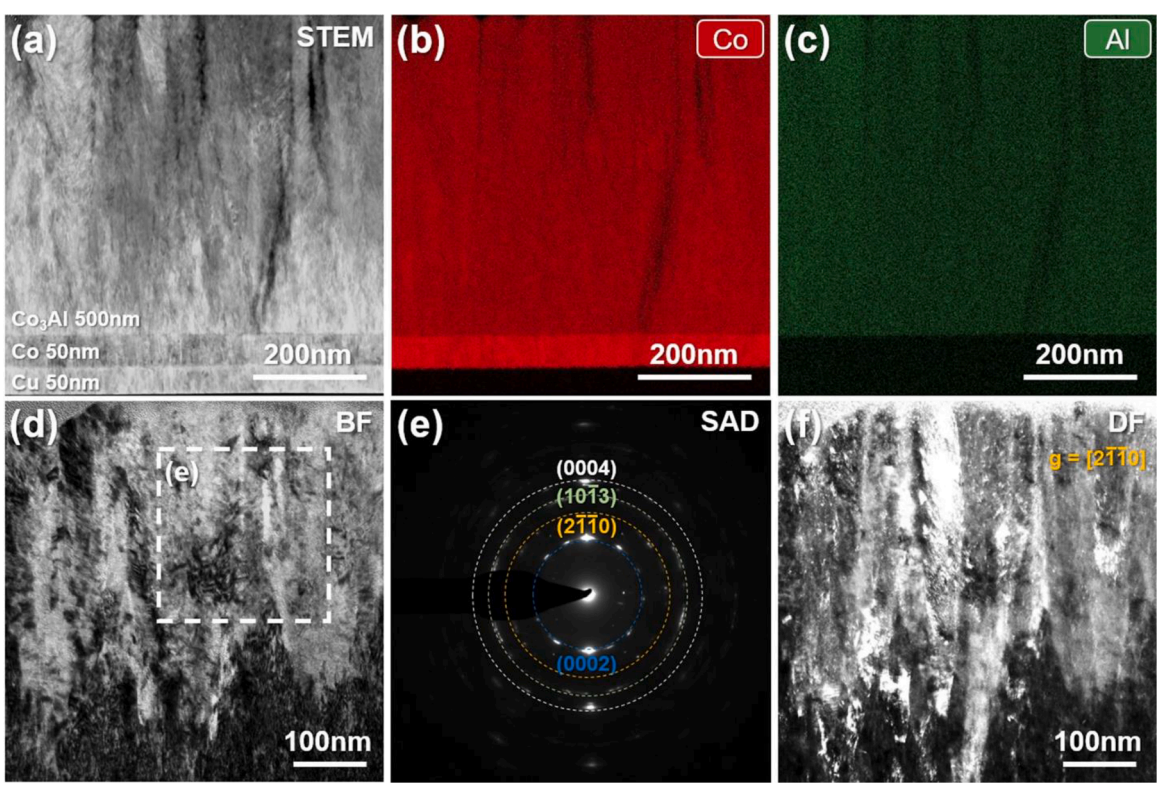

Fig. 2. Cross-section TEM images of as-deposited Co_3Al 500 nm/Co 50 nm/Cu 50 nm stacking on Si (110) substrate. (a) STEM image showing the stacking of layers. (b-c) EDS maps showing the uniform distribution of Co and Al in the co-sputtered Co_3Al layer. (d) BF TEM image of the Co_3Al layer. (e) The corresponding SAD pattern of (e) in (d) is identified as HCP. The discrete diffraction spots indicate strong texture. (f) DF TEM image examined from $g = [2\bar{1}\bar{1}0]$. TEM images were all taken along the Si $[\bar{1}1\bar{1}]$ zone axis.

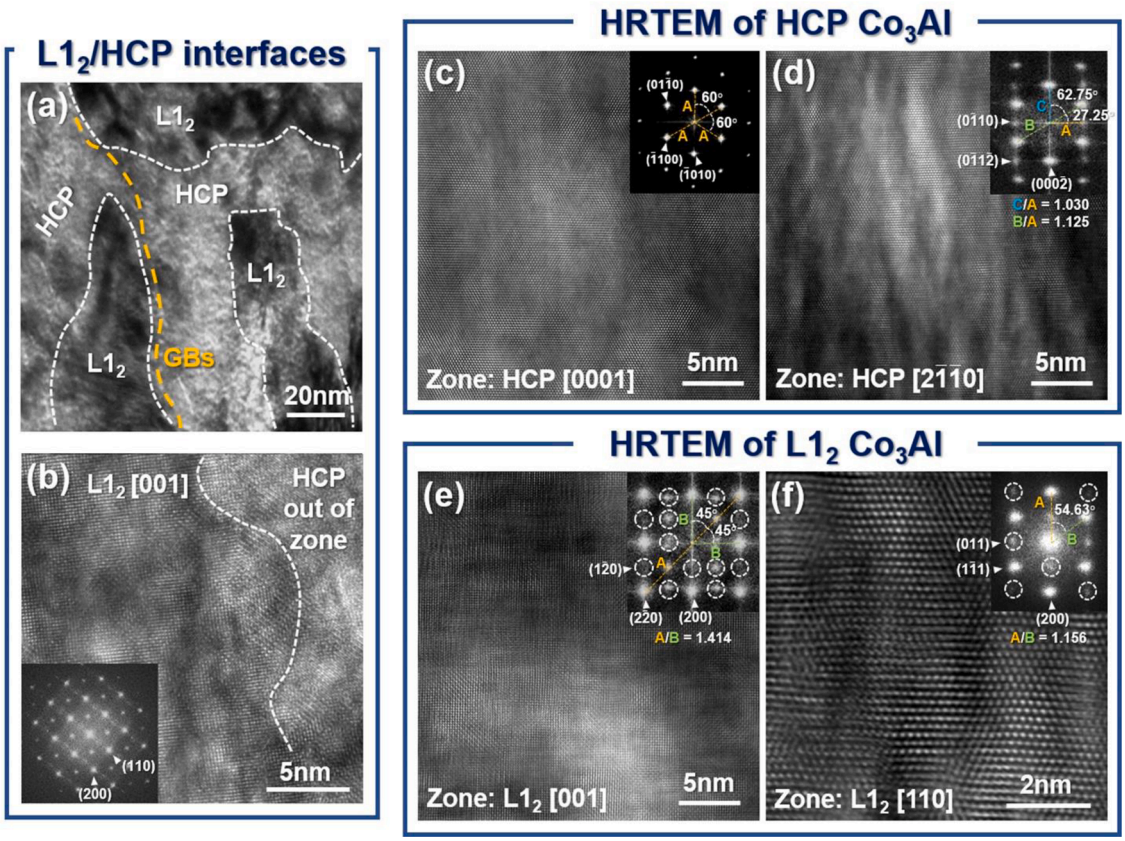

Fig. 3. (a) BF TEM image showing $L1_2$ Co_3Al intermetallics are embedded within HCP Co_3Al supersaturation in the 500 nm thick Co_3Al film. (b) HRTEM image showing interface between $L1_2$ Co_3Al intermetallic and HCP Co_3Al supersaturation. (c, d) HRTEM images and inserted FFTs examined from [0001] and [$2\bar{1}\bar{1}0$] zone axes of HCP Co_3Al. (e, f) HRTEM image and inserted FFT examined from [001] and [110] zone axes of $L1_2$ Co_3Al. The configurations of diffraction patterns were also labelled on the inserted FFTs. The circled spots are superlattice spots in $L1_2$ intermetallic.

radiation to check the texture of as-deposited films. Cross-section TEM specimens were prepared via focused ion beam (FIB) with Pt protection coating on Thermo Fisher Scientific Helios G4 UX dual beam scanning electron microscope (SEM) system equipped with an Omniprobe manipulator. 2 kV low energy Ga^+ ion beam polishing was also carried out to minimize the ion beam damage on sample. TEM and scanning transmission electron microscopy (STEM) studies were conducted on FEI Talos 200X transmission electron microscope operated at 200 kV with a Fischione ultra-high resolution high angle annular dark field (HAADF) detector and a super X energy-dispersive X-ray spectroscopy (EDS) detector.

XRD pattern of the as-deposited 500 nm thick Co_3Al in Fig. 1a reveals strong HCP (0002) texture for Co_3Al on HCP (0002) Co and FCC (111) Cu seed layers. Fig. 1b reveals evident HCP (0002) Co_3Al and HCP (0002) Co textures for 150 nm thick Co/Co_3Al 5 nm multilayers accompanied by the satellite peaks due to the formation of superlattice structure at small layer thickness. The positions of satellite peaks can be calculated by [35]:

$$\frac{2\sin\theta}{\lambda} = \frac{1}{\bar{d}} \pm \frac{n}{h} \tag{1}$$

where λ is the X-ray source wavelength, $\bar{d}$ is the average interplanar spacing, n is the order of satellite peaks, and h is bilayer thickness. The satellite peaks in Fig. 1b can thus be identified as first order superlattice peaks.

Fig. 2a shows the cross-section STEM image of as-deposited Co_3Al 500 nm/Co 50 nm/Cu 50 nm stacking on Si (110) substrate. The corresponding EDS maps in Fig. 2b, c confirm the uniform distribution of Co and Al in the co-sputtered Co_3Al layer. The bright field (BF) TEM image in Fig. 2d reveals the columnar grain morphology in the as-deposited 500 nm thick Co_3Al film. The inserted selected area diffraction (SAD) pattern taken in area (e) in Fig. 2d was indexed to be polycrystalline HCP Co_3Al, and the discrete diffraction spots indicate the formation of strong texture (Fig. 2e). The dark field (DF) TEM image in Fig. 2f taken along the [$2\bar{1}\bar{1}0$] g vector reveals a majority of the columnar grains along vertical growth direction exhibit HCP Co_3Al [$2\bar{1}\bar{1}0$] texture.

Table 1
Comparison of lattice parameters of different crystal structures of Co_3Al and Co.

Source	Chemistry	Approach	Crystal structure	Lattice parameters (Å)
This study	Co_3Al	sputtering	$L1_2$ in Co_3Al 500 nm	$a = 3.633$
This study	Co_3Al	sputtering	HCP in Co_3Al 500 nm	$a = 2.379$, $c = 4.010$
This study	Co_3Al	sputtering	HCP in Co/Co_3Al 5 nm	$a = 2.381$, $c = 4.014$
This study	Co_3Al	sputtering	FCC in Co/Co_3Al 5 nm	$a = 3.476$
Xu et al. [2, 36]	Co_3Al	DFT	$L1_2$	$a = 3.575$ $a = 3.574$
Yang et al. [37]	Co_3Al	DFT	$L1_2$	$a = 3.572$
ICDD [55]	Co	PDF	HCP	$a = 2.503$, $c = 4.061$
ICDD [55]	Co	PDF	FCC	$a = 3.548$

The zoom-in BF TEM image of the 500 nm thick Co_3Al film in Fig. 3a reveals that nano-scale $L1_2$ Co_3Al intermetallics are embedded within the HCP Co_3Al matrix. High-resolution TEM (HRTEM) in Fig. 3b shows the interface between $L1_2$ Co_3Al intermetallic and HCP Co_3Al

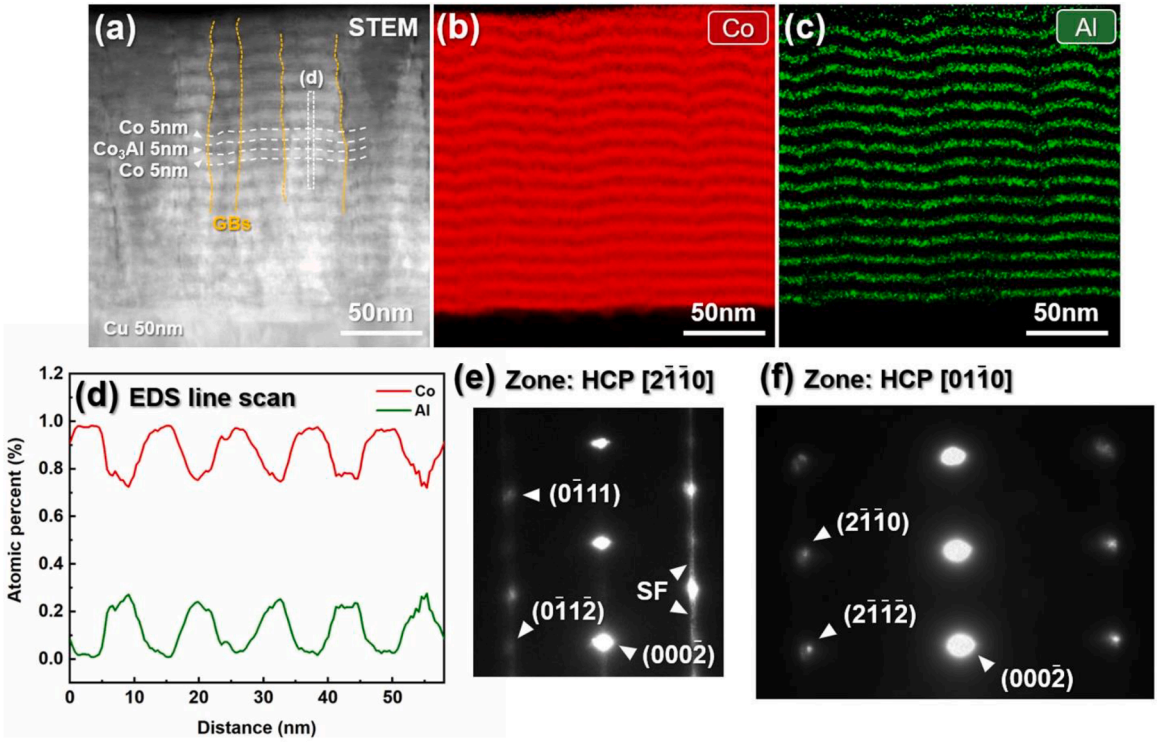

Fig. 4. (a-c) Cross-section STEM and corresponding EDS maps of as-deposited Co/Co_3Al 5 nm multilayers on Cu 50 nm seed layer on Si (110) substrate show abrupt layer interfaces. Images were taken along the Si [$\bar{1}$1$\bar{1}$] zone axis. (d) EDS line scan along the line (d) in (a) shows chemically modulated Co/Co_3Al composition. (e, f) SAD patterns from orthogonal zone axes taken along Si [$\bar{1}$1$\bar{1}$] and Si [1$\bar{1}\bar{2}$] exhibited coherent HCP [2$\bar{1}\bar{1}$0] and [01$\bar{1}$0] for Co/Co_3Al 5 nm multilayers respectively.

supersaturation is not epitaxial. These two metastable crystal structures are verified along two different zone axes via HRTEM images and corresponding Fast Fourier Transform (FFT) analyses in Fig. 3c-f. The calculated lattice parameters of two crystal structures based on our experiments are also summarized in Table 1. It should be noted the calculated lattice parameters of $L1_2$ Co_3Al intermetallics via DFT [2,36] are close to our observations. For example, the calculated lattice parameter from Yang et al. [37] is 3.572 Å, comparing to the experimentally measured value, 3.633 Å. In general, the equilibrium phases of Co-25 at.% Al should be B2 CoAl and HCP Co at room temperature (Fig. S1). How do we account for the formation of metastable and stochiometric Co_3Al phases in the sputtered film? Several potential formation mechanisms of metastable phases of Co_3Al are subsequently discussed.

First, from the thermodynamic point of view, the ultra-high quenching rate of sputtering expands the solubility limit and favors the synthesis of metastable supersaturated phases [38–40]. The formation of HCP Co_3Al supersaturated matrix in our study also supported this argument. Second, the underlying physical mechanisms kinetically governing the formation of metastable phases are surface diffusion, adatom mobility and nucleation [38,21,41]. These physical processes can be varied by tuning the deposition parameters, such as deposition rate, flux ratio between ions and sputtered materials, and Ar ion bombardment through applying substrate bias [38]. When the mobility of sputtered atoms is low, the migration of adatoms to stable nuclei sites is prominently retarded because of the low surface diffusion, thus leading to the preferential nucleation and precipitation of metastable crystals or various microstructure evolution [38,21]. Previous studies on microstructure transformation in the sputtered VAlN film supported this viewpoint by demonstrating the following: (1) formation of metastable FCC VN nanocrystalline grains with amorphous AlN grain boundary distributed phases at lower atomic mobility; (2) formation of metastable single phase FCC (V, Al)N at medium atomic mobility; (3) formation of thermodynamically stable FCC VN and HCP AlN at higher atomic mobility [38]. The formation of $L1_2$ Co_3Al intermetallics in HCP Co_3Al supersaturated matrix during magnetron sputtering, rather than in binary Co-Al bulk systems during casting could be thus illuminated via this theory. The formation of nuclei of metastable ordered phases depends upon atomic mobility and is typically described through critical diffusion distance (X_c) [39]:

$$X_c = \sqrt{\frac{2\mu a_j}{r_D}}\, a_j exp\left(-\frac{Q_D}{2kT_c}\right) \tag{2}$$

where μ is the atomic vibrational frequency, a_j is the individual atom jump distance, r_D is the deposition rate, Q_D is the diffusion activation energy, k is the Boltzmann constant and T_c is the critical temperature at a given r_D. The predicted X_c during room temperature deposition is around one interatomic spacing, significantly less than that for conventional casting and quenching from elevated temperature [39]. Such a low atomic mobility in the sputtering process favors the formation of $L1_2$ Co_3Al intermetallic in our study. We should also consider a third possibility here: the influence of residual stress on the metastable phase formation via ion bombardment [38,41]. Point defects or agglomeration of point defects in form of dislocation loops induced by ion bombardment may alter the residual stress condition inside films, therefore broadening solubility limit and stabilizing supersaturation [42].

In addition to the TEM studies on formation of metastable phases in the single layer Co_3Al, the cross-sectional TEM analyses about the Co/Co_3Al 5 nm multilayers were also conducted. Fig. 4a-c show the STEM image and corresponding EDS maps of multilayer structure. The EDS line scan across several Co/Co_3Al 5 nm multilayers in Fig. 4d indicates the chemically periodic and modulated layer interface without intermixing even at the layer thickness of 5 nm. Fig. 4e, f show the SAD patterns of Co/Co_3Al 5 nm multilayers examined along two orthogonal directions. Only one set of diffraction spots was captured along HCP [2$\bar{1}\bar{1}$0] and [01$\bar{1}$0] respectively, implying the formation of coherent interface in Co/Co_3Al 5 nm multilayers. The vertical streaking lines in

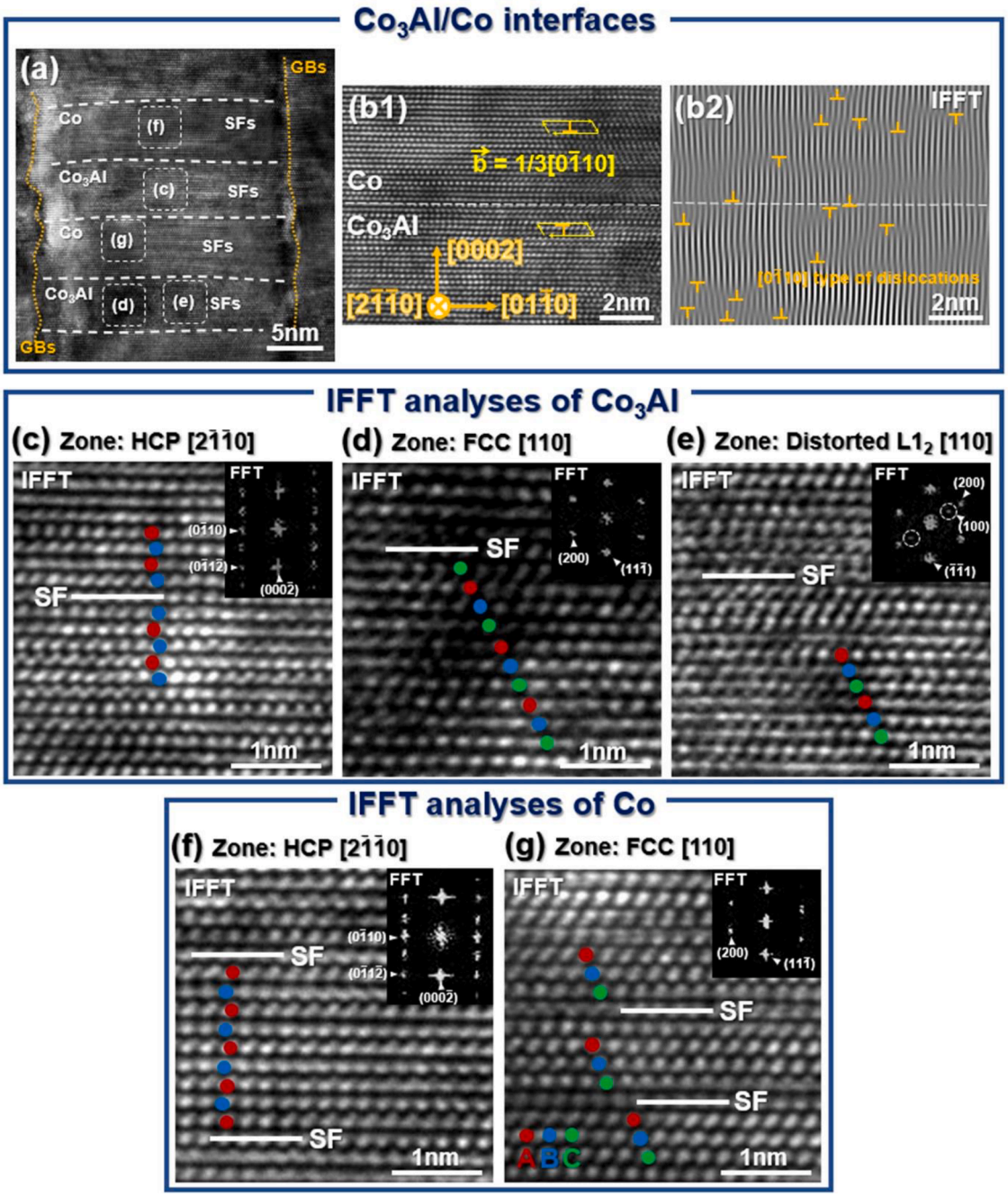

Fig. 5. Cross-section HRTEM of as-deposited Co/Co_3Al 5 nm multilayers. (a) HRTEM image showing high density of SFs in both Co and Co_3Al layers. (b1) Misfit dislocations along Co/Co_3Al interface from HCP [2$\bar{1}\bar{1}$0] zone axis. The Burgers circuit indicates the formation of 1/3 [0$\bar{1}$10] partial dislocation. (b2) IFFT image of (b1) showing locations of [0$\bar{1}$10] type of dislocations. (c-e) IFFT and FFT images of region (c-e) in Co_3Al layers display HCP [2$\bar{1}\bar{1}$0], FCC [110] and distorted $L1_2$ [110] zone axes respectively. (f, g) IFFT and FFT images of region (f, g) in Co layers display HCP [2$\bar{1}\bar{1}$0] and FCC [110] zone axes respectively. SFs were captured in (c-g).

the SAD pattern in Fig. 4e indicate the existence of SFs orthogonal to the growth direction, which is also confirmed in the succeeding HRTEM images.

The cross-sectional HRTEM analyses were performed along HCP [2$\bar{1}\bar{1}$0] zone axis for Co/Co_3Al 5 nm multilayers. Fig. 5a shows the Co/Co_3Al 5 nm multilayers are decorated with a high density of SFs, which are parallel to the basal plane of HCP structure. In contrast, no SFs were captured in the as-deposited 500 nm thick Co_3Al film in Fig. 3. The 1/3 [0$\bar{1}$10] partial misfit dislocations were identified along Co/Co_3Al interface in Fig. 5b1. The Inverse Fast Fourier Transform (IFFT) of Fig. 5b1 reveals the locations of [0$\bar{1}$10] type of dislocations. IFFT of HRTEM images in representative regions (c-g) of both Co and Co_3Al layers in Fig. 5a are presented in Fig. 5c-g. HCP [2$\bar{1}\bar{1}$0], FCC [110] and distorted $L1_2$ [110] zone axes were identified in Co_3Al layers via FFT analyses, and corresponding IFFTs were exhibited in Fig. 5c-e respectively. Similarly, HCP [2$\bar{1}\bar{1}$0] and FCC [110] zone axes were identified in Co layers in Fig. 5f, g. It is noteworthy that the stacking sequences of HCP, FCC and distorted $L1_2$ were intersected frequently by the SFs, implying the SF induced phase transformation between HCP and FCC in both Co and Co_3Al layers. Furthermore, the formation of $L1_2$ Co_3Al intermetallic is also interrupted.

Next, we will attempt to understand the formation mechanisms of

parallel SFs in Co/Co_3Al 5 nm multilayers. First, we consider the formation of misfit dislocations along interfaces between Co and Co_3Al. Interfacial misfit dislocations were identified in Fig. 5b1. The XRD result in Fig. 1b reveals the lattice mismatch between Co (0002) and Co_3Al (0002) is 1.9 % ($d_{Co(0002)} = 2.045$ Å, $d_{Co3Al(0002)} = 2.007$ Å). The critical thickness to form full misfit dislocations (h_c) and partial misfit dislocations (h_p) can be estimated via the following equations [43,44]:

$$h_c = \frac{b}{8\pi f}\cdot\frac{1}{(1+\nu)}\cdot\left(\ln\left(\frac{h_c}{b}\right)+1\right) \tag{3}$$

$$\frac{1}{2}b_p^2 = f h_p b_p \cos\lambda\cdot\frac{2(1+\nu)}{1-\nu} \tag{4}$$

where b is the magnitude of Burgers vector of full misfit dislocation, f is the misfit strain, ν is the average Poisson's ratio, b_p is the magnitude of Burgers vector of partial misfit dislocation and λ is the angle between slip plane and interface. For the case of full misfit dislocation, when b, f and ν are taken as 0.255 nm, 1.9 % and 0.3 respectively [45,12], the calculated h_c is 1.21 nm. In a similar way, for the case of partial misfit dislocation with slip plane parallel to interface, when b_p, f, λ and ν are taken as 0.144 nm, 1.9 %, 0° and 0.3 respectively [45,12], the calculated h_p is 1.02 nm. These estimations are consistent with our experimental observations showing the formation of misfit dislocations along interface between Co/Co_3Al 5 nm multilayers. One should also notice that the formation of misfit dislocation is considered to release the coherency strain [43,46]. When the stored elastic strain energy (induced by interfacial tensile/compressive stress in between Co/Co_3Al multilayers) is sufficient, the formation of misfit dislocations is energetically favored to relieve the coherency strain energy. Second, in HCP metals, the parallel SFs can be generated via the shear of Shockley partials with Burgers vector 1/3 $<10\bar{1}0>$ on the basal plane as it has the lowest energy barrier [24,47–52]. This mechanism is also aligned with the finding of 1/3 $[0\bar{1}10]$ partial misfit dislocations in Fig. 5b1, explaining the formation of parallel SFs in Co_3Al layers.

The periodic slip of Shockley partials (1/3 $<10\bar{1}0>$) and formation of SFs on basal plane in HCP may lead to the HCP-to-FCC phase transformation [24,47–49,53,54], consistent with our experimental observations. This phase transformation can also be seen as a faulted structure. It is also worth mentioning that no perfect $L1_2$ intermetallics were observed in Co_3Al layers, presumably because the consecutive slip of Shockley partials and formation of SFs interrupt the formation of $L1_2$ Co_3Al intermetallic or result in the order-to-disorder transition. The Co/Co_3Al 5 nm multilayers still maintain epitaxial and HCP like features under mesoscale, as shown in the XRD pattern of Fig. 1b and the SAD patterns of Fig. 4e, f, in spite of the frequent coexistence of SFs, indicating the formation of FCC or distorted $L1_2$ phases in the multilayers is localized. The schematic of orientation relationships of HCP, FCC and distorted $L1_2$ phases formed in Co/Co_3Al 5 nm multilayers is shown in Fig. S2b. The calculated lattice parameters of HCP and FCC Co_3Al in Co/Co_3Al 5 nm multilayers are listed in Table 1. One should note that the lattice parameter difference between HCP Co_3Al in Co/Co_3Al 5 nm multilayers and HCP Co_3Al in 500 nm thick single layer is less than 0.1%, which indicates the formation of misfit dislocations along Co/Co_3Al interfaces relieve the corresponding coherency stress. In addition, lattice parameters of HCP and FCC Co_3Al are both lower than those of HCP and FCC Co (extracted from powder diffraction file (PDF) cards in International Center for Diffraction Data (ICDD) database) as shown in Table 1, implying the shrinkage of lattice unit cell after the formation of Co_3Al supersaturation.

We report the finding of several intriguing metastable crystal structures of sputtered Co_3Al in this work. The primary HCP Co_3Al supersaturated matrix and secondary $L1_2$ Co_3Al intermetallics were identified in the as-deposited Co_3Al single layer film via transmission electron microscopy. In comparison, the HCP-to-FCC Co_3Al phase transformation induced by Shockley partials and SFs was captured in the as-deposited Co/Co_3Al 5 nm multilayers. The consecutive SFs interrupted the formation of $L1_2$ Co_3Al and resulted in the order-to-disorder transition. The experimentally measured lattice parameters of metastable Co_3Al phases were also listed. The measured lattice parameter of $L1_2$ Co_3Al intermetallic is close to the DFT calculations. Our investigations shed light on formation mechanisms of metastable Co_3Al phases and provide new perspectives for the design of novel Co-Al based alloy systems.

CRediT authorship contribution statement

Ke Xu: Conceptualization, Investigation, Methodology, Validation, Visualization, Writing – original draft. **Zhongxia Shang:** Data curation, Investigation, Methodology, Writing – review & editing. **Xuanyu Sheng:** Data curation, Methodology, Visualization, Writing – review & editing. **Nicholas Richter:** Formal analysis, Methodology, Visualization, Writing – review & editing. **Anyu Shang:** Data curation, Formal analysis, Methodology, Writing – review & editing. **Chao Shen:** Data curation, Formal analysis, Visualization, Writing – review & editing. **Bo Yang:** Data curation, Methodology, Writing – review & editing. **Yifan Zhang:** Data curation, Formal analysis, Validation, Visualization, Writing – review & editing. **Tongjun Niu:** Data curation, Formal analysis, Validation, Writing – review & editing. **Haiyan Wang:** Formal analysis, Methodology, Supervision, Writing – review & editing. **Xinghang Zhang:** Conceptualization, Funding acquisition, Resources, Supervision, Writing – review & editing.

Declaration of competing interest

The authors declare that they have no known competing financial interests or personal relationships that could have appeared to influence the work reported in this paper.

Acknowledgement

The authors acknowledge financial supports from NSF-DMR-2210152. XS is supported by DOE-BES under grant No. DE-SC0016337. H.W. acknowledges the support from the U.S. Office of Naval Research (N00014-22-1-2160). We are also thankful to discussions with Dr. Yashashree Kulkarni and Anand Mathew from Department of Mechanical Engineering, University of Houston.

Supplementary materials

Supplementary material associated with this article can be found, in the online version, at doi:10.1016/j.scriptamat.2024.116184.

References

[1] S.K. Makineni, M.P. Singh, K. Chattopadhyay, Low-Density, High-Temperature Co Base Superalloys, Annu. Rev. Mater. Res. 51 (2021) 187–208, https://doi.org/10.1146/annurev-matsci-080619-014459.

[2] W.W. Xu, S.L. Shang, C.P. Wang, T.Q. Gang, Y.F. Huang, L.J. Chen, X.J. Liu, Z. K. Liu, Accelerating exploitation of Co-Al-based superalloys from theoretical study, Mater. Des. 142 (2018) 139–148, https://doi.org/10.1016/j.matdes.2018.01.013.

[3] B.X. Cao, W.-W. Xu, C.Y. Yu, S.W. Wu, H.J. Kong, Z.Y. Ding, T.L. Zhang, J.H. Luan, B. Xiao, Z.B. Jiao, Y. Liu, T. Yang, C.T. Liu, L12-strengthened multicomponent Co-Al-Nb-based alloys with high strength and matrix-confined stacking-fault-mediated plasticity, Acta Mater. 229 (2022) 117763, https://doi.org/10.1016/j.actamat.2022.117763.

[4] W.-W. Xu, Z.Y. Xiong, X.G. Gong, G.H. Yin, L.J. Chen, C.P. Wang, X.J. Liu, Accelerating the discovery of novel γ/γ' Co-based superalloys by probing temperature and alloying effects on the γ' precipitates, Materialia 18 (2021) 101171, https://doi.org/10.1016/j.mtla.2021.101171.

[5] Y. Chen, C. Wang, J. Ruan, S. Yang, T. Omori, R. Kainuma, K. Ishida, J. Han, Y. Lu, X. Liu, Development of low-density γ/γ' Co–Al–Ta-based superalloys with high solvus temperature, Acta Mater. 188 (2020) 652–664, https://doi.org/10.1016/j.actamat.2020.02.049.

[6] Y. Chen, C. Wang, J. Ruan, T. Omori, R. Kainuma, K. Ishida, X. Liu, High-strength Co–Al–V-base superalloys strengthened by γ'-Co3(Al,V) with high solvus temperature, Acta Mater. 170 (2019) 62–74, https://doi.org/10.1016/j.actamat.2019.03.013.

[7] B. Liao, X. Ouyang, H. Li, F. Yin, Z. Li, B. Yin, J. Hu, W. Zhang, Experimental investigation and thermodynamic calculation of the Co-Al-Mo ternary system, J. Alloys Compd. 945 (2023) 169114, https://doi.org/10.1016/j.jallcom.2023.169114.

[8] Y. Li, H. Long, X. Zhang, S. Shi, P. Sang, Z. Zhang, Multi-phase-field simulation of D019-χ transformation in Co-Al-W superalloy with L12-γ′ + fcc-γ phases, Comput. Mater. Sci. 230 (2023) 112445, https://doi.org/10.1016/j.commatsci.2023.112445.

[9] A. Suzuki, H. Inui, T.M. Pollock, L12-strengthened cobalt-base superalloys, Annu. Rev. Mater. Res. 45 (2015) 345–368, https://doi.org/10.1146/annurev-matsci-070214-021043.

[10] S.K. Makineni, B. Nithin, D. Palanisamy, K. Chattopadhyay, Phase evolution and crystallography of precipitates during decomposition of new "tungsten-free" Co (Ni)–Mo–Al–Nb γ–γ′ superalloys at elevated temperatures, J. Mater. Sci. 51 (2016) 7843–7860, https://doi.org/10.1007/s10853-016-0026-1.

[11] M.P. Singh, S.K. Makineni, K. Chattopadhyay, Achieving lower mass density with high strength in Nb stabilised γ/γ′ Co–Al–Mo–Nb base superalloy by the replacement of Mo with V, Mater. Sci. Eng.A 794 (2020) 139826, https://doi.org/10.1016/j.msea.2020.139826.

[12] M. Jin, N. Miao, W. Zhao, J. Zhou, Q. Du, Z. Sun, Structural stability and mechanical properties of Co3(Al, M) (M = Ti, V, Cr, Zr, Nb, Mo, Hf, Ta, W) compounds, Comput. Mater. Sci. 148 (2018) 27–37, https://doi.org/10.1016/j.commatsci.2018.02.015.

[13] H. Ali, R. Chen, H. Chen, Y. Zhao, P. Zhao, S. Yang, B. Wu, J. Wen, C. Zhang, L. Weng, T. Xie, Q. Cai, L. Zhang, Z. He, Q. Yao, H. Zhang, B. Sa, C. Wen, M. Lin, Y. Liu, C. Wang, The ordering behavior of Co3Al-based γ′ phase with L12 structure predicted by the thermodynamic model with support of first-principles calculations, Mater. Today Commun. 33 (2022) 104447, https://doi.org/10.1016/j.mtcomm.2022.104447.

[14] B.O. Mukhamedov, S. Fritze, M. Ottosson, B. Osinger, E. Lewin, B. Alling, U. Jansson, I.A. Abrikosov, Tetragonal distortion in magnetron sputtered bcc-W films with supersaturated carbon, Mater. Des. 214 (2022) 110422, https://doi.org/10.1016/j.matdes.2022.110422.

[15] P.-P. Wu, G.-L. Song, Y.-X. Zhu, Z.-L. Feng, D.-J. Zheng, The corrosion of Al-supersaturated Mg matrix and the galvanic effect of secondary phase nanoparticles, Corros. Sci. 184 (2021) 109410, https://doi.org/10.1016/j.corsci.2021.109410.

[16] T. Yi, M. Yang, N. Li, P. Xing, Z. He, F. Zheng, K. Du, B. Ke, Y. Liu, Microstructure and resistivity of Au-B supersaturated solid-solution films prepared by sputter deposition, Thin Solid Films 758 (2022) 139431, https://doi.org/10.1016/j.tsf.2022.139431.

[17] S. Fritze, M. Chen, L. Riekehr, B. Osinger, M.A. Sortica, A. Srinath, A.S. Menon, E. Lewin, D. Primetzhofer, J.M. Wheeler, U. Jansson, Magnetron sputtering of carbon supersaturated tungsten films – A chemical approach to increase strength, Mater. Des. 208 (2021) 109874, https://doi.org/10.1016/j.matdes.2021.109874.

[18] S. Fritze, M. Hans, L. Riekehr, B. Osinger, E. Lewin, J.M. Schneider, U. Jansson, Influence of carbon on microstructure and mechanical properties of magnetron sputtered TaW coatings, Mater. Des. 196 (2020) 109070, https://doi.org/10.1016/j.matdes.2020.109070.

[19] D. Pravarthana, O.I. Lebedev, A. David, A. Fouchet, M. Trassin, G.S. Rohrer, P. A. Salvador, W. Prellier, Metastable monoclinic [110] layered perovskite $Dy_2Ti_2O_7$ thin films for ferroelectric applications, RSC Adv. 9 (2019) 19895–19904, https://doi.org/10.1039/c9ra04554f.

[20] W. Fang, W. Zhu, Y. Shao, P. Zheng, J. Si, Formation of metastable cubic phase and thermoelectric properties in Mg3Bi2 films deposited by magnetron sputtering, Appl. Surf. Sci. 596 (2022) 153602, https://doi.org/10.1016/j.apsusc.2022.153602.

[21] S. Chen, J. Wang, R. Wu, Z. Wang, Y. Li, Y. Lu, W. Zhou, P. Hu, H. Li, Insights into the nucleation, grain growth and phase transformation behaviours of sputtered metastable β-W films, J. Mater. Sci. Technol. 90 (2021) 66–75, https://doi.org/10.1016/j.jmst.2021.02.027.

[22] M. Červená, R. Čerstvý, T. Dvořák, J. Rezek, P. Zeman, Metastable structures in magnetron sputtered W–Zr thin-film alloys, J. Alloys Compd. 888 (2021) 161558, https://doi.org/10.1016/j.jallcom.2021.161558.

[23] J.W. Yan, X.F. Zhu, G.P. Zhang, C. Yan, Evaluation of plastic deformation ability of Cu/Ni/W metallic multilayers, Thin Solid Films 527 (2013) 227–231, https://doi.org/10.1016/j.tsf.2012.11.052.

[24] Y.F. Zhang, S. Xue, Q. Li, J. Li, J. Ding, T.J. Niu, R. Su, H. Wang, X. Zhang, Size dependent strengthening in high strength nanotwinned Al/Ti multilayers, Acta Mater. 175 (2019) 466–476, https://doi.org/10.1016/j.actamat.2019.06.028.

[25] R. Su, D. Neffati, Q. Li, S. Xue, J. Cho, J. Li, J. Ding, Y. Zhang, C. Fan, H. Wang, Y. Kulkarni, X. Zhang, Ultra-high strength and plasticity mediated by partial dislocations and defect networks: part I: texture effect, Acta Mater. 185 (2020) 181–192, https://doi.org/10.1016/j.actamat.2019.11.049.

[26] C. Zhou, J. Wang, J. Meng, W. Li, P. Liu, K. Zhang, F. Ma, X. Ma, R. Feng, P.K. Liaw, Effects of modulation layer thickness on fracture toughness of a TiN/AlN-Ni multilayer film, Mater. Des. 222 (2022) 111097, https://doi.org/10.1016/j.matdes.2022.111097.

[27] B. Zuo, J. Xu, G. Lu, H. Ju, L. Yu, Microstructures, mechanical properties and corrosion resistance of TiN/AlN multilayer films, Ceram. Int. 48 (2022) 11629–11635, https://doi.org/10.1016/j.ceramint.2022.01.020.

[28] N. Kumar, A.V. Nezhdanov, S.A. Garakhin, P.A. Yunin, V.N. Polkovnikov, N. I. Chkhalo, A.I. Mashin, Microstructure and phonon behavior in W/Si periodic multilayer structures, J. Phys. D Appl. Phys. 55 (2022) 175302, https://doi.org/10.1088/1361-6463/ac4729.

[29] J. Li, Y. Chen, S. Xue, H. Wang, X. Zhang, Comparison of size dependent strengthening mechanisms in Ag/Fe and Ag/Ni multilayers, Acta Mater. 114 (2016) 154–163, https://doi.org/10.1016/j.actamat.2016.05.030.

[30] B. Ham, X. Zhang, High strength Mg/Nb nanolayer composites, Mater. Sci. Eng. A 528 (2011) 2028–2033, https://doi.org/10.1016/j.msea.2010.10.101.

[31] M. Jain, N. Velisavljevic, J.K. Baldwin, M. Knezevic, N.A. Mara, I.J. Beyerlein, S. Pathak, Structure and properties of pseudomorphically transformed bcc Mg in Mg/Nb multilayered nanolaminates studied using synchrotron X-ray diffraction, J. Appl. Phys. 126 (2019) 025302, https://doi.org/10.1063/1.5097249.

[32] B.M. Clemens, H. Kung, S.A. Barnett, Structure and Strength of Multilayers, MRS Bull. 24 (1999) 20–26, https://doi.org/10.1557/S0883769400051502.

[33] N. Koutná, L. Löfler, D. Holec, Z. Chen, Z. Zhang, L. Hultman, P.H. Mayrhofer, D. G. Sangiovanni, Atomistic mechanisms underlying plasticity and crack growth in ceramics: a case study of AlN/TiN superlattices, Acta Mater. 229 (2022) 117809, https://doi.org/10.1016/j.actamat.2022.117809.

[34] H. Kung, Y.-C. Lu, A.J. Griffin Jr., M. Nastasi, T.E. Mitchell, J.D. Embury, Observation of body centered cubic Cu in Cu/Nb nanolayered composites, Appl. Phys. Lett. 71 (1997) 2103–2105, https://doi.org/10.1063/1.119611.

[35] E.E. Fullerton, I.K. Schuller, H. Vanderstraeten, Y. Bruynseraede, Structural refinement of superlattices from x-ray diffraction, Phys. Rev. B 45 (1992) 9292–9310, https://doi.org/10.1103/PhysRevB.45.9292.

[36] W.W. Xu, J.J. Han, Z.W. Wang, C.P. Wang, Y.H. Wen, X.J. Liua, Z.Z. Zhu, Thermodynamic, structural and elastic properties of Co3X (X = Ti, Ta, W, V, Al) compounds from first-principles calculations, Intermetallics 32 (2013) 303–311, https://doi.org/10.1016/j.intermet.2012.08.022.

[37] C. Yang, X. Yu, Y. Chen, J. Han, X. Liu, C. Wang, Enhancing structural stability of γ′-Co3(Al, Nb) phases: the key role of anti-site defects, Mater. Des. 232 (2023) 112117, https://doi.org/10.1016/j.matdes.2023.112117.

[38] M. Stüber, S. Ulrich, H. Leiste, H. Holleck, Magnetron sputtered nanocrystalline metastable (V,Al)(C,N) hard coatings, Surf. Coat. Technol. 206 (2011) 610–616, https://doi.org/10.1016/j.surfcoat.2011.07.052.

[39] B. Cantor, R.W. Cahn, Metastable alloy phases by co-sputtering, Acta Metallurgica 24 (1976) 845–852, https://doi.org/10.1016/0001-6160(76)90051-1.

[40] K. Chang, D. Music, M. to Baben, D. Lange, H. Bolvardi, J.M. Schneider, Modeling of metastable phase formation diagrams for sputtered thin films, Sci. Technol. Adv. Mater. 17 (2016) 210–219, https://doi.org/10.1080/14686996.2016.1167572.

[41] S. Liu, K. Chang, D. Music, X. Chen, S. Mráz, D. Bogdanovski, M. Hans, D. Primetzhofer, J.M. Schneider, Stress-dependent prediction of metastable phase formation for magnetron-sputtered V1−xAlxN and Ti1−xAlxN thin films, Acta Mater. 196 (2020) 313–324, https://doi.org/10.1016/j.actamat.2020.06.044.

[42] G. Håkansson, J.-E. Sundgren, D. McIntyre, J.E. Greene, W.-D. Münz, Microstructure and physical properties of polycrystalline metastable Ti0.5Al0.5N alloys grown by d.c. magnetron sputter deposition, Thin Solid Films 153 (1987) 55–65, https://doi.org/10.1016/0040-6090(87)90169-6.

[43] Y. Liu, Y. Chen, K.Y. Yu, H. Wang, J. Chen, X. Zhang, Stacking fault and partial dislocation dominated strengthening mechanisms in highly textured Cu/Co multilayers, Int. J. Plast. 49 (2013) 152–163, https://doi.org/10.1016/j.ijplas.2013.03.005.

[44] J.W. Matthews, A.E. Blakeslee, Defects in epitaxial multilayers: I. Misfit dislocations, J. Cryst. Growth 27 (1974) 118–125, https://doi.org/10.1016/S0022-0248(74)80055-2.

[45] P. Liu, D. Chen, Q. Wang, P. Xu, M. Long, H. Duan, Crystal structure and mechanical properties of nickel–cobalt alloys with different compositions: a first-principles study, J. Phys. Chem. Solids 137 (2020) 109194, https://doi.org/10.1016/j.jpcs.2019.109194.

[46] Y. Liu, D. Bufford, H. Wang, C. Sun, X. Zhang, Mechanical properties of highly textured Cu/Ni multilayers, Acta Mater. 59 (2011) 1924–1933, https://doi.org/10.1016/j.actamat.2010.11.057.

[47] A.C. Redfield, A.M. Zangwill, Stacking sequences in close-packed metallic superlattices, Phys. Rev. B 34 (1986) 1378–1380, https://doi.org/10.1103/PhysRevB.34.1378.

[48] R.M. Wood, The lattice constants of high purity alpha titanium, Proc. Phys. Soc. 80 (1962) 783, https://doi.org/10.1088/0370-1328/80/3/323.

[49] H. Li, D.E. Mason, T.R. Bieler, C.J. Boehlert, M.A. Crimp, Methodology for estimating the critical resolved shear stress ratios of α-phase Ti using EBSD-based trace analysis, Acta Mater. 61 (2013) 7555–7567, https://doi.org/10.1016/j.actamat.2013.08.042.

[50] B. Li, Q. Sun, X.Y. Zhang, Lattice correspondence analysis on the formation mechanism for partial stacking faults in hexagonal close-packed metals, Comput. Mater. Sci. 198 (2021) 110684, https://doi.org/10.1016/j.commatsci.2021.110684.

[51] S.Q. Zhu, S.P. Ringer, On the role of twinning and stacking faults on the crystal plasticity and grain refinement in magnesium alloys, Acta Mater. 144 (2018) 365–375, https://doi.org/10.1016/j.actamat.2017.11.004.

[52] R. Su, D. Neffati, J. Cho, Q. Li, J. Ding, H. Wang, Y. Kulkarni, X. Zhang, Phase transformation induced plasticity in high-strength hexagonal close packed Co with stacking faults, Scr. Mater. 173 (2019) 32–36, https://doi.org/10.1016/j.scriptamat.2019.07.030.

[53] G.P. Zheng, Molecular dynamics and first-principles studies on the deformation mechanisms of nanostructured cobalt, J. Alloys Compd. 504 (2010) S467–S471, https://doi.org/10.1016/j.jallcom.2010.02.144.
[54] G.P. Zheng, Y.M. Wang, M. Li, Atomistic simulation studies on deformation mechanism of nanocrystalline cobalt, Acta Mater. 53 (2005) 3893–3901, https://doi.org/10.1016/j.actamat.2005.04.038.
[55] S. Gates-Rector, T. Blanton, The Powder Diffraction File: a quality materials characterization database, Powder Diffr. 34 (2019) 352–360, https://doi.org/10.1017/S0885715619000812.